RAMAN-BASED MEASUREMENTS OF GREENHOUSE ACTIVITY OF COMBUSTION FLUE GASES

BY

FARZAN KAZEMIFAR

THESIS

Submitted in partial fulfillment of the requirements
for the degree of Master of Science in Mechanical Engineering
in the Graduate College of the
University of Illinois at Urbana-Champaign, 2011

Urbana, Illinois

Adviser:

Associate Professor Dimitrios C. Kyritsis

Abstract

Gases that are capable of absorbing and emitting infrared radiation due to their molecular structure are known as infrared active gases. Infrared activity is the underlying reason for the greenhouse effect. Hence, greenhouse gases are all infrared active. The vibrational/rotational structure that makes the molecule infrared active, also causes the energy exchange and the corresponding wavelength shift during Raman scattering.

In this work, Raman scattering spectrum and infrared emission intensity in CO_2-containing atmospheric jets at various temperatures and concentrations were measured. The results show that there is a linear relationship between Raman scattering intensity and infrared emission intensity. The linear relationship between Raman signal and infrared emission intensity indicates that Raman scattering can be used as a strong technique for measurement of greenhouse gases.

Acknowledgement

Firstly, I would like to express my sincere appreciation to my adviser Dr. Dimitrios Kyritsis for guiding and helping me through this path that turned out not to be a very smooth one. His patience and positive attitude when things would not go as planned definitely had a great effect in helping me complete this work. I also would like to thank Dr. Qunxing Huang for his ideas, comments and performing the computer simulations.

I owe thanks to my fellow labmates: David Tse, David Schmidt, Dino Mitsingas, Sangkyoung Lee, Michael Pennisi, Ben Wigg, Chris Evans and Maria Agathou. I have been lucky to work with such a great group.

Last but not least I want to express my gratitude to my parents, family and friends for their love and support throughout my life.

Table of Contents

Chapter 1: Introduction....1

1.1 Infrared Activity.... 1

1.2 Raman Scattering 3

1.3 Motivation for This Thesis....7

Chapter 2: Experimental Setup....8

2.1 Raman Spectroscopy....10

2.2 Infrared Imaging....12

Chapter 3: Infrared Emission....14

Chapter 4: Raman Scattering....21

Chapter 5: Summary, Conclusions and Recommendations....34

5.1 Summary and Conclusions....34

5.2 Recommendations for Future Work....35

References....37

Chapter 1: Introduction

The work presented in this thesis is focused primarily on Raman scattering from greenhouse gases. This chapter provides a brief overview of the literature on the greenhouse effect, infrared activity and the correlation between greenhouse potential and Raman scattering.

1.1 Infrared Activity

Greenhouse gases are gases that are capable of emitting/absorbing photons in the infrared range of electromagnetic radiation. For this reason, they are also referred to as infrared-active gases. The reason that they are called "greenhouse" gases is that they bring about the "greenhouse effect" in earth's atmosphere.

Figure 1.1 shows spectral distribution of solar radiation at the top of the atmosphere (extraterrestrial radiation) as well as at the earth's surface [1]. The difference between the two indicates absorption by atmospheric gases such as H_2O, CO_2, and O_3.

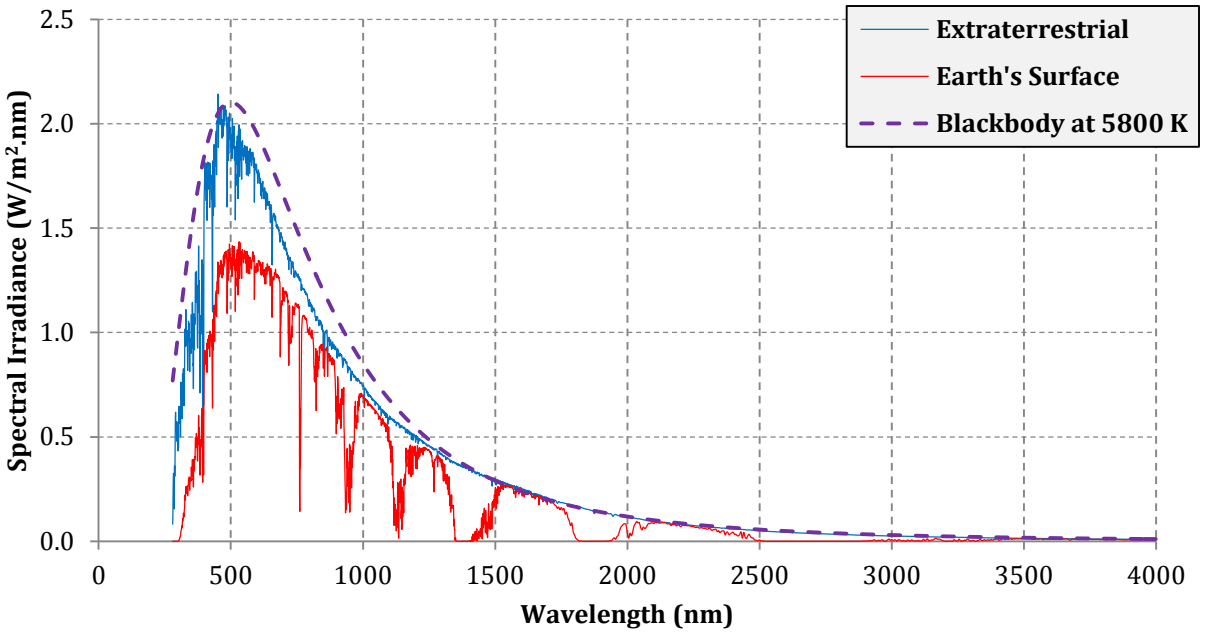

Figure 1.1 – Spectral Distribution of Solar Radiation

As shown in Fig. 1.1, solar radiation spectrum is very similar to a blackbody at 5800 K and has its peak spectral irradiance in the visible light range of the spectrum (close to 550 nm). Thus, the amount of absorption by infrared-active gases in the atmosphere will be relatively small. A large fraction of sun's radiative energy that passes through the atmosphere is absorbed by earth's surface, thus warming it up. According to Wien's law, due to earth's surface temperature, the peak spectral irradiance will be in the infrared region (near 10 μm). Infrared-active gases absorb part of the radiative energy from the earth that would have otherwise passed through the atmosphere and entered the outer space. Part of this absorbed energy is reemitted back to earth, absorbed by earth and reemitted by earth. This creates a cycle that results in heat being trapped in earth's atmosphere. This phenomenon is referred to as the "greenhouse effect", which is the mechanism that is responsible both for the habitable conditions on our planet, and at the same time, for recent concerns about climate change [2].

The underlying reason for this behavior is the vibrational structure of the molecules. Not all molecules are infrared-active. In order for a molecule to be infrared-active its electric dipole moment should change with the vibration of the atoms of the molecule, which is the case for CO, CO_2, H_2O and CH_4 that are the most relevant greenhouse gases. On the other hand, O_2, N_2, H_2 as well as any other diatomic homonuclear molecule are not infrared-active. During absorption/emission of an infrared photon, the molecule transitions to a vibrational state with higher/lower energy. The energy difference between the initial and the final state is exactly equal to the energy of the absorbed/emitted photon. This energy difference is a characteristic of the molecule and is used for detecting different species [3, 4].

1.2 Raman Scattering

Spontaneous Raman scattering is the phenomenon of inelastic scattering of photons of light by molecules and has significant applications in laser diagnostics. This phenomenon, like infrared activity, also stems from the vibrational structure of the molecules. In this phenomenon, the molecule absorbs the energy of a photon and transitions to a virtual higher energy state. Through emitting a photon the molecule goes to a lower energy state, which is different from the initial state. As a result, the scattered radiation experiences a shift in frequency with respect to the incident radiation. This frequency shift is a characteristic of the irradiated molecule, which makes Raman scattering species specific [5, 6]. If the final state is higher than the initial state, the frequency shift will be negative and the phenomenon is called Stokes Raman scattering (energy is transferred from the photon to the molecule). On the other hand, if the final state is lower than the initial state, the

frequency shift will be positive and the phenomenon is called anti-Stokes Raman scattering (energy is transferred from the molecule to the photon). Figure 1.2 shows a schematic diagram of Raman scattering and infrared emission/absorption.

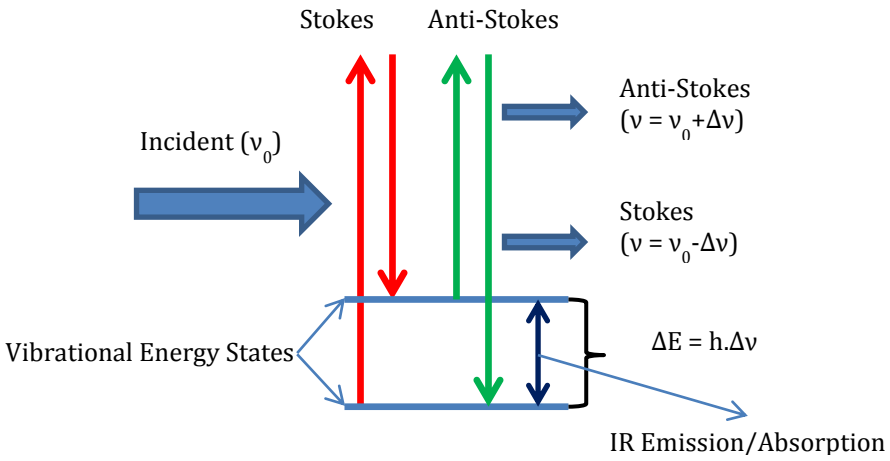

Figure 1.2 – Raman scattering
h: Planck constant, ν: Frequency

In order for a molecule to have vibrational Raman spectrum, its polarizability must change as the molecule vibrates. This constitutes a slight difference from infrared activity for which dipole moment, not polarizability has to change. As a result, almost all of the species of a combustion process, even those that are not infrared-active, do have at least one Raman-active mode; and this includes CO, CO_2, H_2O, CH_4, H_2, N_2, O_2, etc. [3-5]. Figure 1.2 illustrates the close relation between Raman and infrared spectroscopy. Thus, Raman scattering can be used to measure the infrared activity of the gases resulting from a combustion process in order to assess the greenhouse potential of the gases present.

Raman scattering has several advantages over other combustion diagnostic techniques. One being the fact that only one excitation wavelength is sufficient in order to monitor all of

the species under consideration. Visible and ultraviolet (UV) lasers are most commonly used in order to exploit the fact that Raman scattering signal intensity scale as the fourth power of frequency [5]. However, visible light laser was employed in almost all previous combustion-related works [7-23] in order to avoid fluorescence interference from a possible UV excitation. The other advantage is that Raman scattering occurs in a time on the order of 10^{-12} seconds which is essentially instantaneous compared to fluorescence (in laser induced fluorescence, LIF) that has a lifetime of 10^{-10}-10^{-5} seconds [5]. Nevertheless, the most important advantage of Raman scattering is that in general (most of the time but not always) there is little overlap in vibrational Raman spectra of different species[1] [6]. However, the biggest disadvantage of Raman scattering that limits its applicability to some extent, despite all the advantages mentioned above, is the weakness of Raman scattering signal. In fact, Raman cross sections of various species are typically several orders of magnitude smaller than their fluorescence and Rayleigh cross sections [5, 6]. The weakness of the signal poses a great experimental challenge for efficient collection of Raman scattering signal.

Despite the difficulties and complexities involved in Raman scattering signal collection, this method has been extensively used in combustion diagnostics. D. A. Stephenson measured high-temperature (1000-2200 K) Raman spectra of CO_2 and H_2O for use in combustion studies [7]. D. P. Aeschliman and colleagues used Raman scattering to study hydrogen diffusion flame in air. They obtained time-averaged, spatially resolved measurements of temperature and H_2, N_2 and O_2 concentration. [8]. R. J. Blint and D. A. Stephenson measured

[1] Note that this is true only for vibrational Raman scattering and not for rotational Raman scattering.

temperature and CO_2 concentration in methane-air flames. They concluded that temperature measurements from CO_2 Raman spectrum is in agreement with but less accurate than temperature measurements using N_2 spectrum [9]. S. M. Schoenung and R. E. Mitchell, measured temperatures in ammonia-oxygen flames using Raman spectroscopy and compared the results with thermocouple readings. Their results indicated that care must be taken when analyzing measured intensities obtained in flames with species fluorescing in the Raman spectra region [10].

M. B. Long and colleagues performed two-dimensional (2-D) measurements of species using different techniques. They employed Mie scattering to obtain 2-D concentration measurements in seeded turbulent non-reacting jet [11]. They also used Raman scattering to obtain 2-D distribution of D_2 concentration in a turbulent D_2/Air diffusion flame and CH_4 concentration in a non-reacting turbulent jet [12]. Moreover, they employed Raman and Rayleigh scattering simultaneously to obtain 2-D mapping of temperature and CH_4 concentration in turbulent CH_4 flames (both premixed and non-premixed) [13].

D.C. Kyritsis and colleagues established the feasibility of quantitative, 2-D, single-shot Raman measurements of methane concentration. They obtained quantitative 2-D Raman measurements of methane concentration in a laminar methane jet into nitrogen. They also obtained 2-D, instantaneous, quantitative measurements of hydrogen concentration in an optically accessible pressurized chamber [14, 15].

R. S. Barlow, A. N. Karpetis and colleagues used Raman scattering along with Laser Induced Fluorescence (LIF) and Rayleigh scattering with several lasers and ICCD cameras to measure temperature, mixture fraction and scalar dissipation in turbulent flames. Raman scattering was used to measure major combustion species such as O_2, N_2, CO_2, H_2O and H_2 [16-20].

1.3 Motivation for this Thesis

Despite the extensive use of Raman scattering in combustion diagnostics, this method has not yet been used for the purpose of measuring infrared activity and greenhouse potential in an environment where there is no combustion or flame; i.e. flue gas stream of thermal power plants that use fossil fuels. In fact, due to the absence of background luminosity, such measurements are less challenging than those performed in flames. This work presents preliminary data on feasibility of such measurements.

This work will present the behavior of Raman scattering intensity and infrared emission intensity as functions of temperature and composition. Infrared emission results will be compared to computational data. The infrared emission data and Raman scattering measurements are compared in order to establish a quantitative correlation between the two signals.

Chapter 2: Experimental Setup

A schematic of the experimental apparatus is shown in Fig. 2.1. Greenhouse-gas-containing mixtures with controlled composition were metered through a steel tube heater. The heated gas then emerged as an atmospheric jet. The inner and outer diameter of the tube was 1.5 and 2 inch respectively and the length of the tube was 1 m. The tube was heated by a radiative heater from ZIRCAR Ceramics, Inc. The heater consisted of a ceramic shell, with an inner diameter of 8 cm, containing an electric heating coil. The power of the heater was controlled by varying its voltage using a potentiometer and varied between 0 and 1400 W.

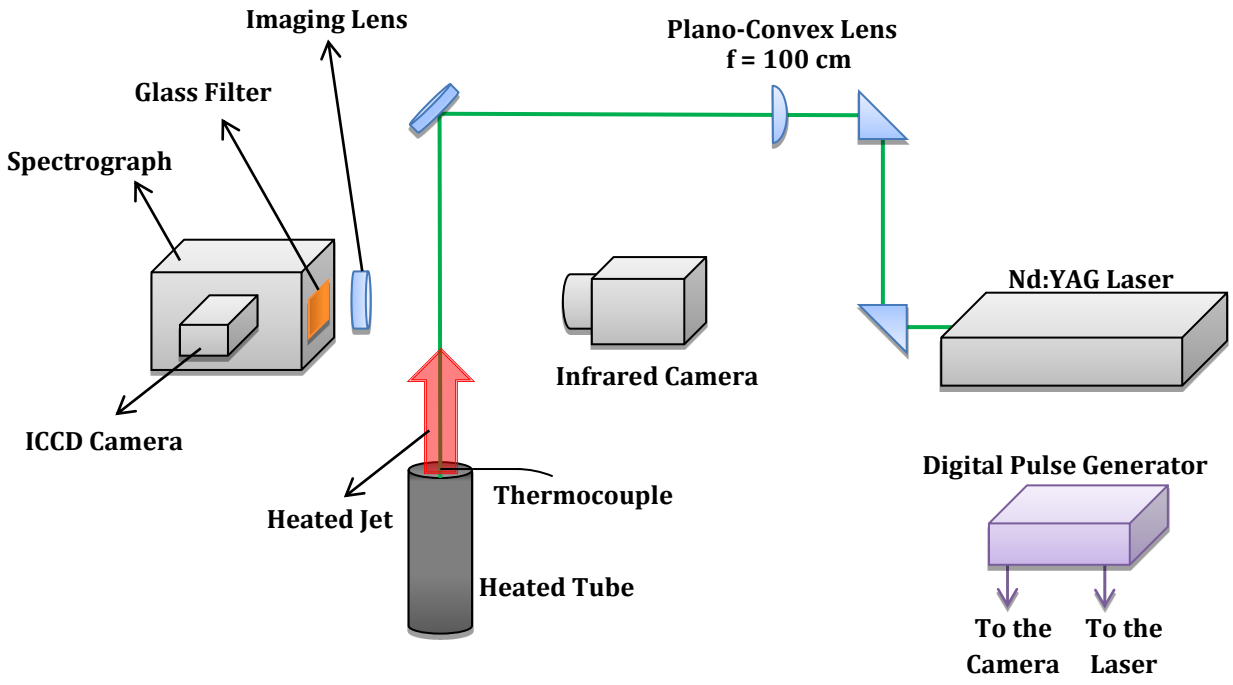

Figure 2.1 – Experimental setup

The greenhouse gas studied in the experiment was CO_2. Nitrogen was the gas that was mixed with CO_2 in order to vary CO_2 concentration at constant pressure. The mole-fraction range that was tested was 5-40% CO_2 and it was scanned with a 5% increment in mole-fraction. The flow rates were controlled by two Tylan General FC-320 mass flow controllers that were controlled by a Tylan General RO-28 control unit. The total flow rate was kept constant at 30 SLPM. The reason for having such a relatively high flow rate was to have a jet with high enough velocity and momentum that was inertially driven not affected by the drafts in ambient air and by buoyancy that is unavoidable in this configuration. In order to figure out the significance of buoyancy forces, Gr/Re^2 was calculated, as suggested in [24]. The mixture was considered to be an ideal gas. The diameter of the tube and the length of the tube were the length scales used for Reynolds number and Grashof number respectively. Based on these assumptions:

$$\frac{Gr_L}{Re_D^2} = \frac{g(T_s - T_\infty)L^3}{T_\infty V^2 D^2}$$

Where g is the gravity acceleration, T_s is the tube surface temperature, T_∞ is the temperature of the gas, L is the length of the tube, D is the inner diameter of the tube and V is the velocity of the gas. Neither the gas temperature nor the tube wall temperature was constant along the tube. In order to get an estimate, $T_s - T_\infty$ and T_∞ were assumed to be 100 K and 600 K. The calculations yielded $Gr/Re^2 \approx 1400 >> 1$, which indicates that the jets were driven by buoyancy forces.

As mentioned above, the power of the heater could be varied, and this was used in order to control the temperature of the gas. A K-type thermocouple was used to measure the

temperature of the gas. It was placed in a way that its tip was at the center of the exit plane of the tube. Radiation shielding was not used for this thermocouple.

2.1 Raman Spectroscopy

The second harmonic (532 nm) of a Quanta-Ray Pro-250 Nd:YAG laser with maximum nominal output of 800 mJ per pulse was used as an excitation source. The laser was triggered at 10 Hz using a four-channel Stanford Research Systems DG535 digital delay/pulse generator. The laser was operated at half of its maximum power, and was run for a minimum of 30 minutes before the experiment in order to reach steady state where the power did not change with time. The laser power was measured at about 25 cm above the probe volume, using a Scientech AC2501 calorimeter. The power measured was 0.50±0.01 W throughout the experiment. This corresponds to 50 mJ/pulse and is substantially smaller than the power at the laser output, because of significant losses in the prisms in the beam path. It was not possible to measure the laser beam power at the probe volume without damaging the detector, because, the energy density was too large due to focusing, but there is no reason to believe that this figure would change drastically.

Using a plano-convex lens with a focal length of 1 m the laser beam was focused to an approximately 2 mm wide and 4 cm long vertical line. It was attempted to make the laser beam coincide with the tube/jet axis, however, this was not achieved completely because of the complexities involved in aligning the laser beam in an optical setup with 3 prisms, 1 mirror and 1 lens. Although the beam did not coincide perfectly with the jet axis, it is safe to say that it was within 1 cm of the jet axis.

A 50 mm Nikon f#1.8 lens was used for signal collection. Dispersion was achieved using a 68 mm×68 mm grating with 1200 grooves/mm and 300 nm blaze wavelength mounted on the triple grating turret in an Acton Research 300i imaging spectrograph with a focal length of 300 mm. An Anodr iStar DH734-18F-A3 intensified-CCD camera, with a CCD chip having 1024×1024 pixels with a pixel size of 13 μm was used for recording the spectra. The camera was mounted at the exit plane of the spectrograph in a way that the image plane of the spectrograph coincided with the CCD plane of the camera.

In order to reject Rayleigh, Mie scattered and stray reflected light, an OG 550, 3 mm thick glass filter was placed in front of the slit of the spectrograph. The slit opening of the spectrograph was set at 0.25 mm.

The image intensifier of the camera was a Gen III intensifier whose diameter was 18 mm and had a gating speed of 5 ns in the ultra-fast mode. The intensifier was equipped with a glass window and a Type EVS photocathode with P43 phosphor and had a spectral range of 270-810 nm. The readout speeds of the controller card were 1, 2, 16 and 32 μs per pixel. In order to synchronize the camera and the laser, the camera was triggered using the same digital delay/pulse generator that was used for triggering the laser. Data acquisition was performed with a PC using the Andor Solis software. For each point of measurement, the exposure time of the camera was set to minimum (0.002 s) and the image intensifier was gated for 100 ns in order to minimize interference. 300 such exposures were accumulated on the CCD before readout to improve the signal-to-noise ratio.

2.2 Infrared Imaging

Infrared emission was detected and measured using an Electrophysics PV320L infrared camera. The camera was equipped with a 50 mm, f#1.0 germanium lens that was transparent in the 2-14 μm range of the spectrum. The resolution of this camera was 320×240 pixels. Data acquisition was performed by converting the analog video output from the camera to digital using a StarTech USB 2.0 Video Capture Cable and a PC.

Infrared radiation from hot metal surfaces is much stronger than the infrared radiation from greenhouse gases. A hot metal surface in the viewing area of the camera could affect the accuracy of results negatively. In such a case, the relatively weak emission from the gas (especially at low temperature and concentration) will not be easily distinguishable from the background when a very strong source of emission is present. For this reason, the camera was positioned in a way that the metal tip of the thermocouple and the hot steel tube were not in the viewing area. Figure 2.2 shows the viewing area of the infrared camera with respect to the heated tube, thermocouple and the hot jet.

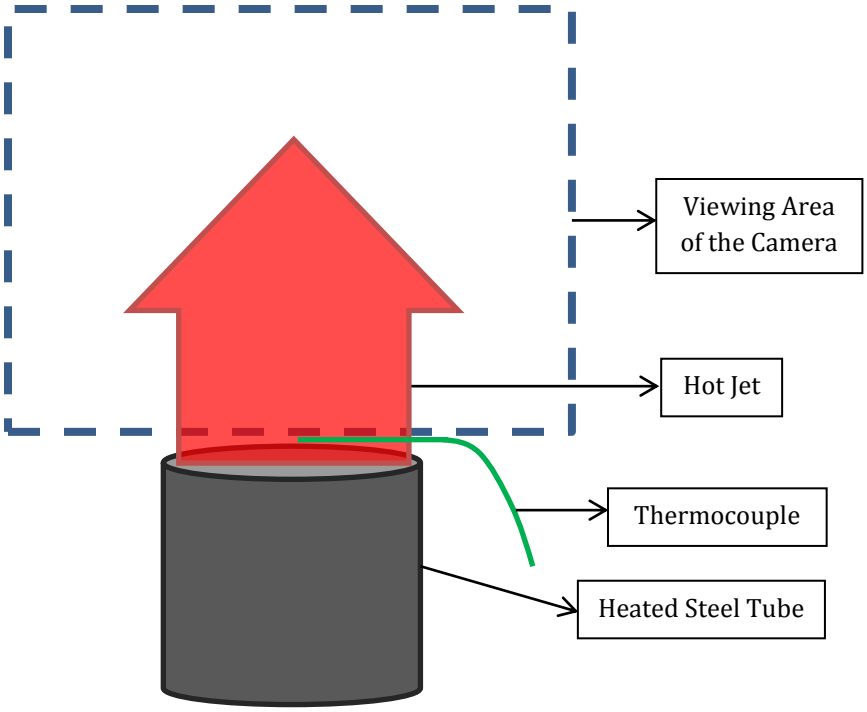

Figure 2.2 – Viewing area of the infrared camera with respect to the thermocouple, heated tube and the jet

Chapter 3: Infrared Emission

CO_2 is an infrared active gas, which means that it can emit/absorb photons in the infrared region. The strongest infrared emission/absorption bands of CO_2 are at 667.3, 2349.3, 3609, 3716 cm^{-1} that correspond to 15.0, 4.26, 2.77 and 2.69 μm respectively [25]. Fig. 3.1 presents CO_2 absorption bands. The infrared camera that we used was able to detect wavelengths in the 2-14 μm range.

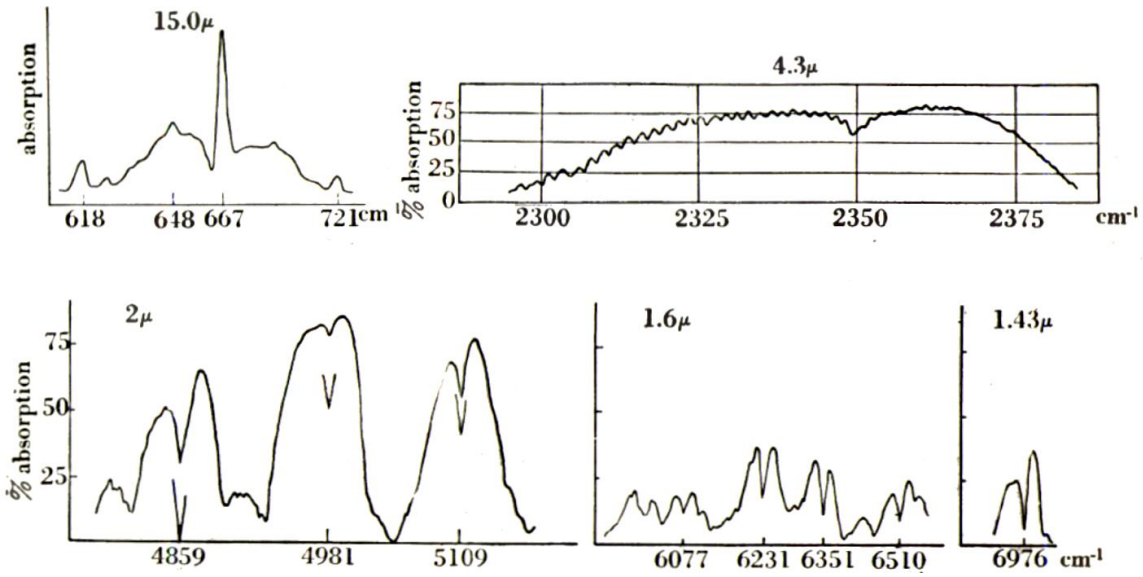

Figure 3.1 – CO_2 infrared absorption spectrum [25]

Given that the infrared camera was able to detect wavelengths in the range of 2-14 μm, the output basically consisted of the sum of infrared emissions from 2.69, 2.77 and 4.26 μm bands. The output of the camera was interlaced 8-bit grayscale images. As an example, Fig. 3.2 shows the output of the camera for emission from a 40%-molar CO_2/N_2 mixture at 250°C.

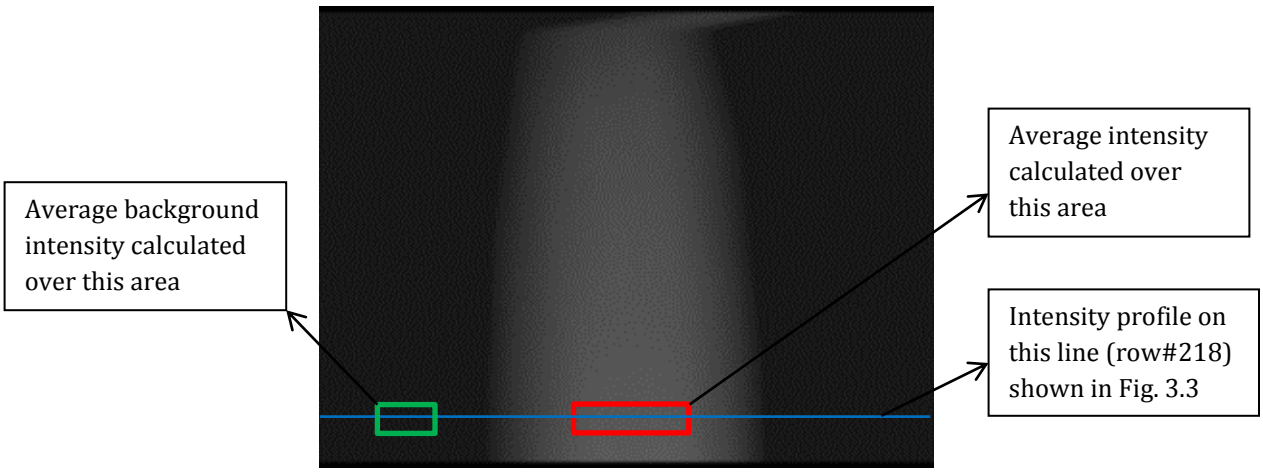

Figure 3.2 – Infrared Camera Output for 40% CO_2 by Volume at 250°C

Figure 3.3 shows the intensity profile on row#218 of the image (blue line shown in Fig. 3.2) as well as the average over rows 210-225, with background subtracted. In the following paragraph, the method used for determining the background intensity is explained.

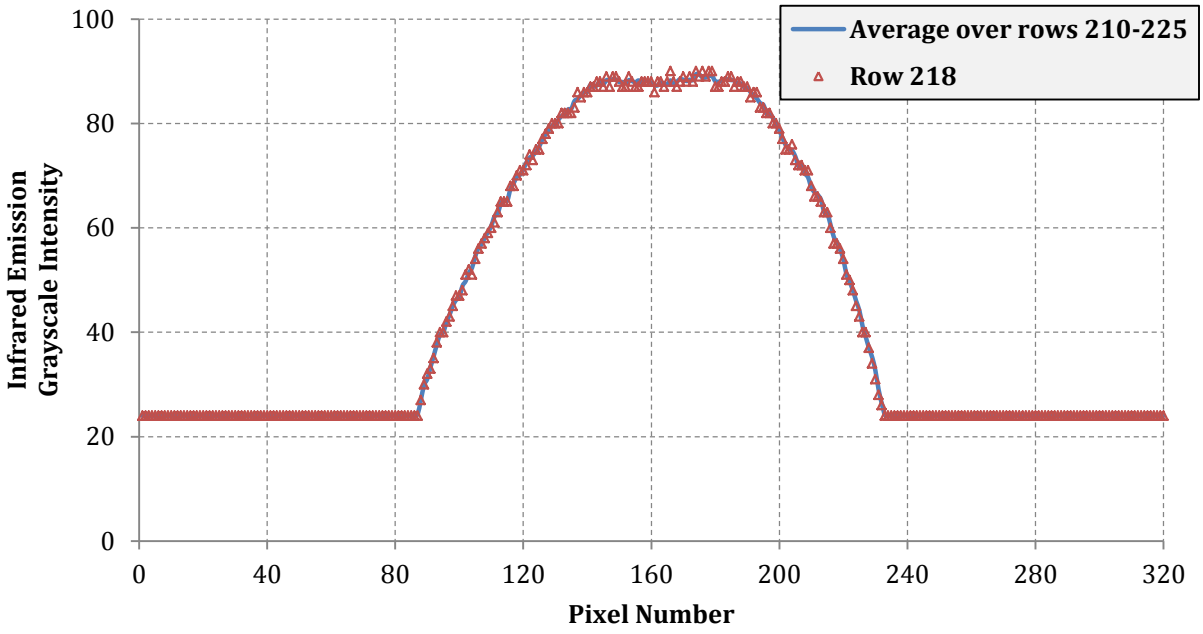

Figure 3.3 – Infrared Emission Profile

According to Fig. 3.3, the emission intensity profile is symmetric about the axis of the jet, and there is little difference between the averaged profile and single-row profile. The results also show that the emission intensity profile has a flat maximum in the center of the jet (pixels 130-190). For this reason, the average pixel value over a 60×15 pixel area (red rectangle shown in Fig. 3.2) was used as the raw signal for measurements in different cases. Also, in order to calculate the average background intensity, an area away from the jet was chosen. For this purpose, the average pixel value over a 30×15 pixel area (green rectangle shown in Fig. 3.2) was used as the background intensity, which was subtracted from the raw signal in order to account for the effects of background infrared radiation.

Figures 3.4 and 3.5 report results of infrared measurements. As shown in Fig. 3.4, the relationship between intensity and concentration is linear to a very good approximation. In Fig. 3.5, fourth order polynomials are fit to the data. These polynomials represent the relationship between infrared emission and temperature quite accurately, with R^2 values very close to unity. The reason for choosing fourth-order polynomials was the fourth-power dependence of Stefan-Boltzmann blackbody radiation on temperature.

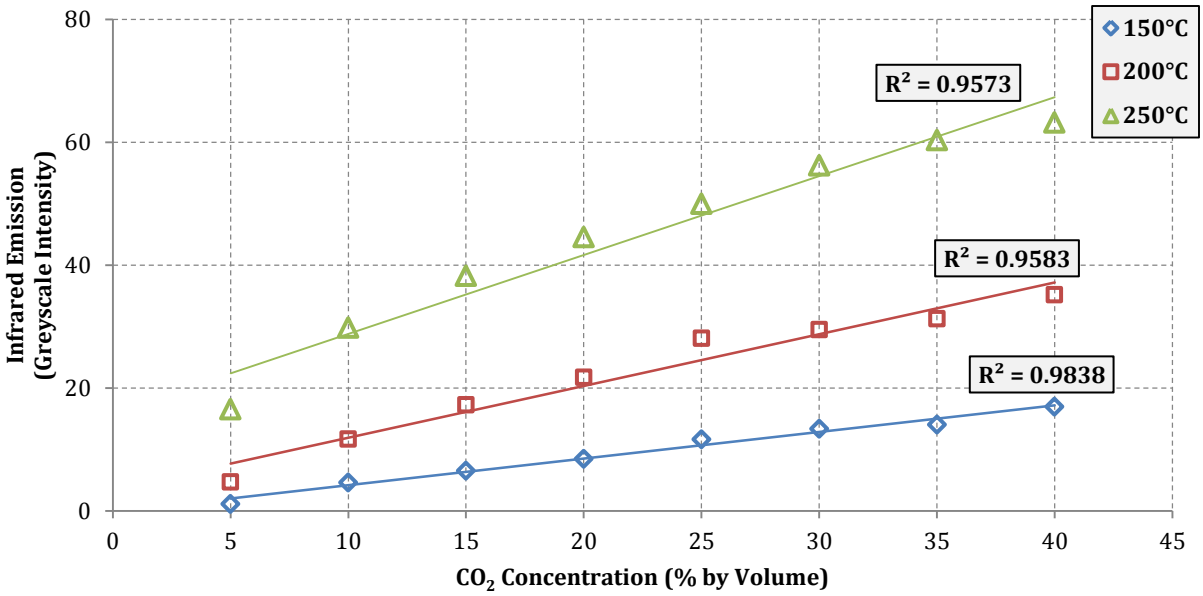

Figure 3.4 – Infrared Emission Intensity vs. Concentration for CO_2

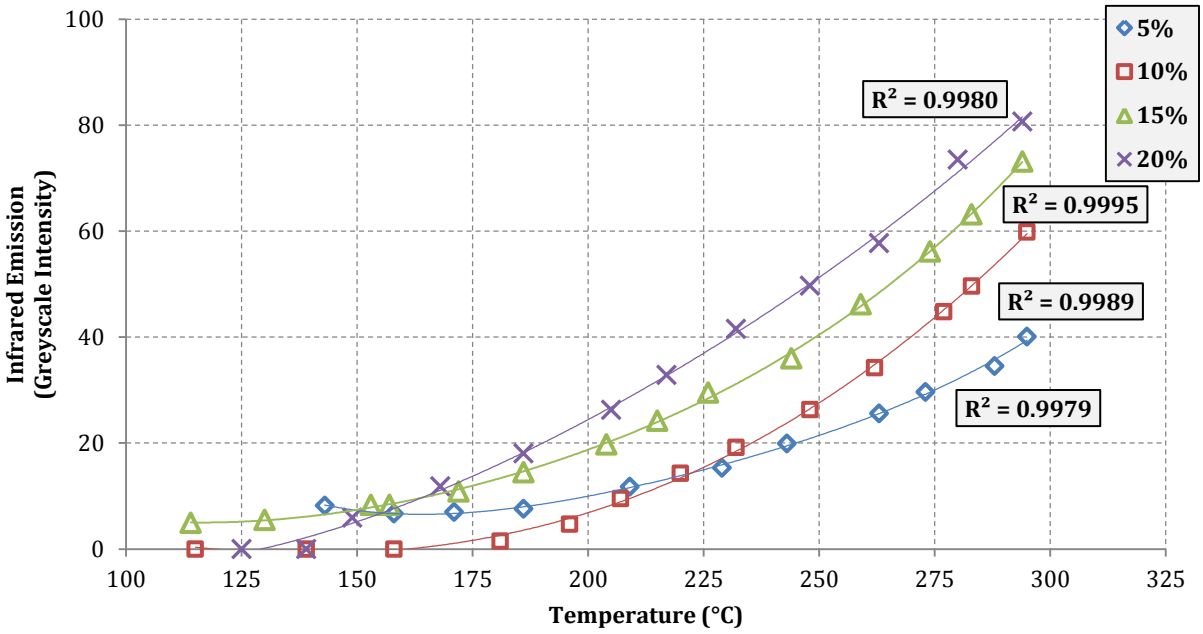

Figure 3.5 – Infrared Emission Intensity vs. Temperature for CO_2

Figures 3.6 and 3.7 compare the experimental results with simulations performed using the RADCAL code published by the National Institute of Standards and Technology [26]. The computations include the 2.0, 2.7, 4.3 and 10 μm emission bands. The code uses a narrowband model for calculating infrared emissions. This model uses a harmonic

oscillator approximation to calculate band intensities, and anharmonicity is brought into account to compute the spectral distribution. These calculations were done by Professor Quinxing Huang who is a visiting professor from Institute of Thermal Power Engineering of ZJU in China at University of Illinois at Urbana-Champaign. The data points and the lines correspond to experimental results and the simulation results respectively.

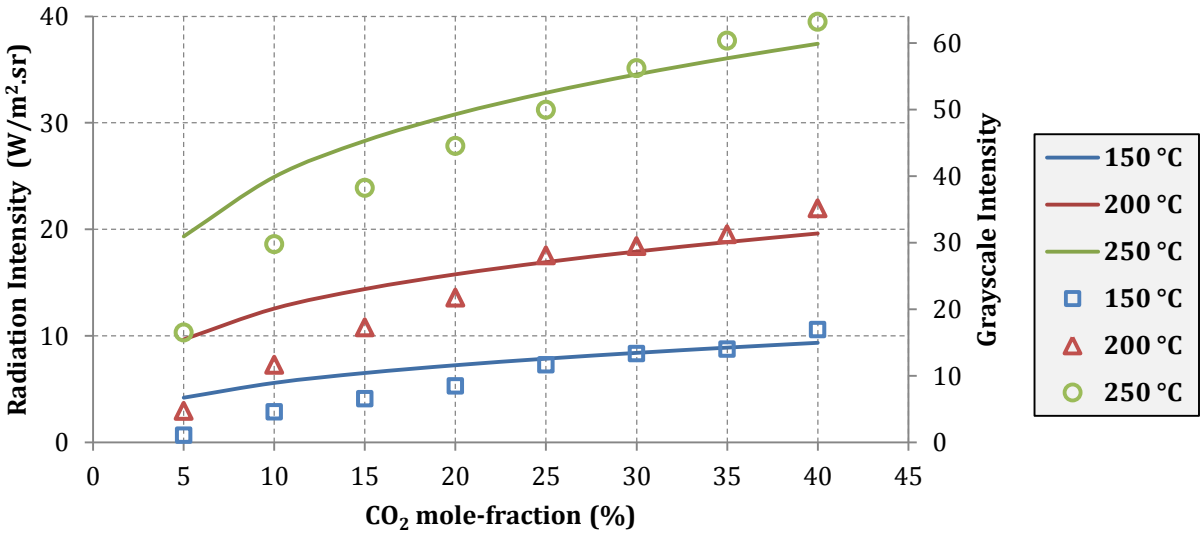

Figure 3.6 – Experimental and Numerical Results Comparison for Infrared Emission Intensity vs. CO_2 mole fraction

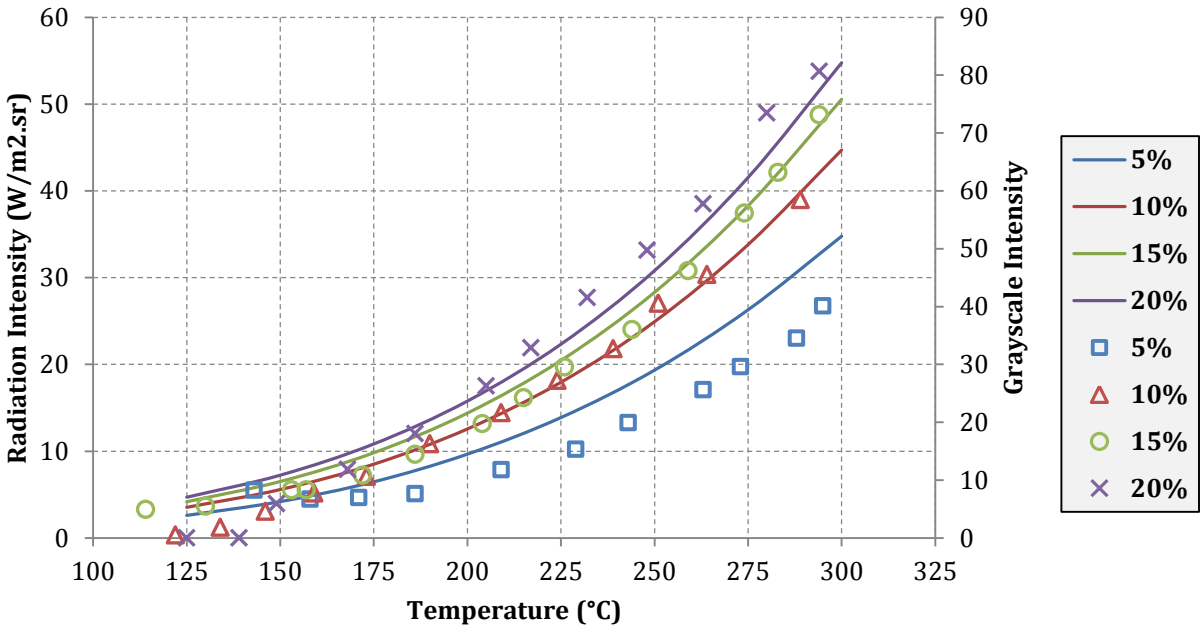

Figure 3.7 – Experimental and Numerical Results Comparison for Infrared Emission Intensity vs. Temperature

The experimental measurements of CO_2 emission agree closely with the numerical simulations in most situations. Nevertheless, the agreement is not perfect and especially at lower concentrations, the difference between experiment and simulation is noticeable. This result could be caused by low sensitivity of the camera as well as nonlinearity of the response of the camera to radiation intensity. Figure 3.8 shows infrared emission results for a CO_2 mole fraction of 10% from two separate measurements. At low temperatures where the measured emission intensity was almost zero there was not much difference between the sets of data. This was also true about the high end of the temperature range. Nevertheless, the difference was noticeable in the mid-temperature range around 200°C. This comparison, gives us a qualitative image of the uncertainty of the infrared emission measurements.

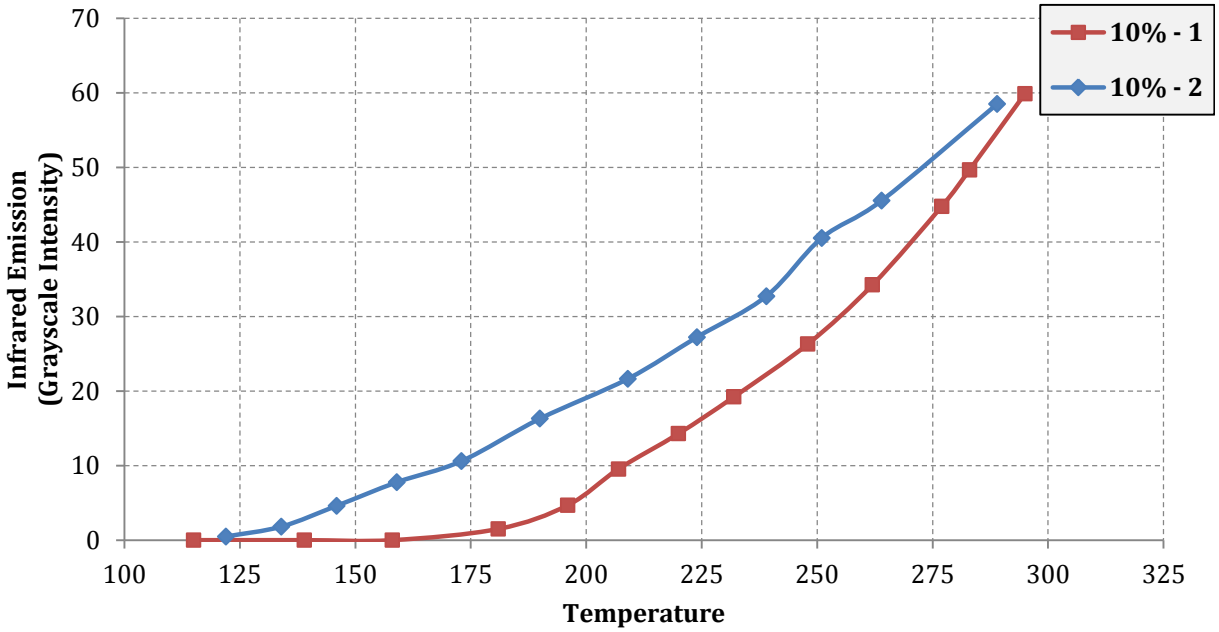

Figure 3.8 –Infrared Emission Measurements for 10% CO_2 by volume

Chapter 4: Raman Scattering

In the vibrational Raman spectrum of CO_2 molecule, under low resolution, there is one strong band at 1340 cm^{-1}, which corresponds to the symmetric stretch of the carbon oxygen bond. However, under higher dispersion it becomes evident that this strong band really consists of two lines at 1285 cm^{-1} and 1388 cm^{-1}. This phenomenon is due to the vibrational structure of the molecule that causes a Fermi resonance which in turn leads to the occurrence of two almost equally intense Raman lines –instead of one [25]. So, since the exciting laser wavelength was 532 nm, the Stokes peaks were expected to occur at 571 nm and 574.4 nm.

The spectra recorded on the spectrograph were processed in order to determine the effect of temperature and concentration on the spectra in the manner that will be described here. Figure 4.1 shows the spectrum obtained for a 20%-CO_2-by-volume jet at 104°C as an example. Figure 4.1b presents the same data as Fig. 4.1a over a narrower range of wavelengths in order to focus on the peaks.

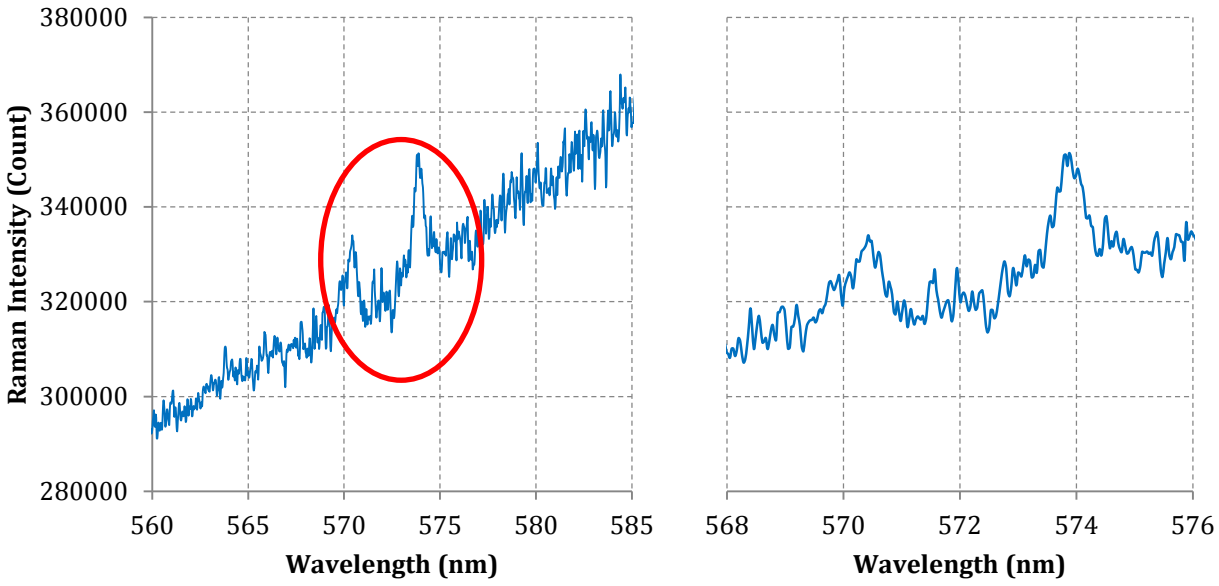

(a) (b)

Figure 4.1 – Raman spectrum (20% CO_2 by volume at 104°C)

In order to smooth the spectrum and account for the camera noise, 10, 20 and 40-point average of the spectrum were taken. Figure 4.2 shows the actual spectrum and the smoothed spectra. A 10-point average was the one that was chosen to be applied as a compromise between noise reduction and spectrum resolution. As shown in the results, the 10-point average merely smoothed out the fluctuations of the spectrum without causing any significant change in the peak width and height.

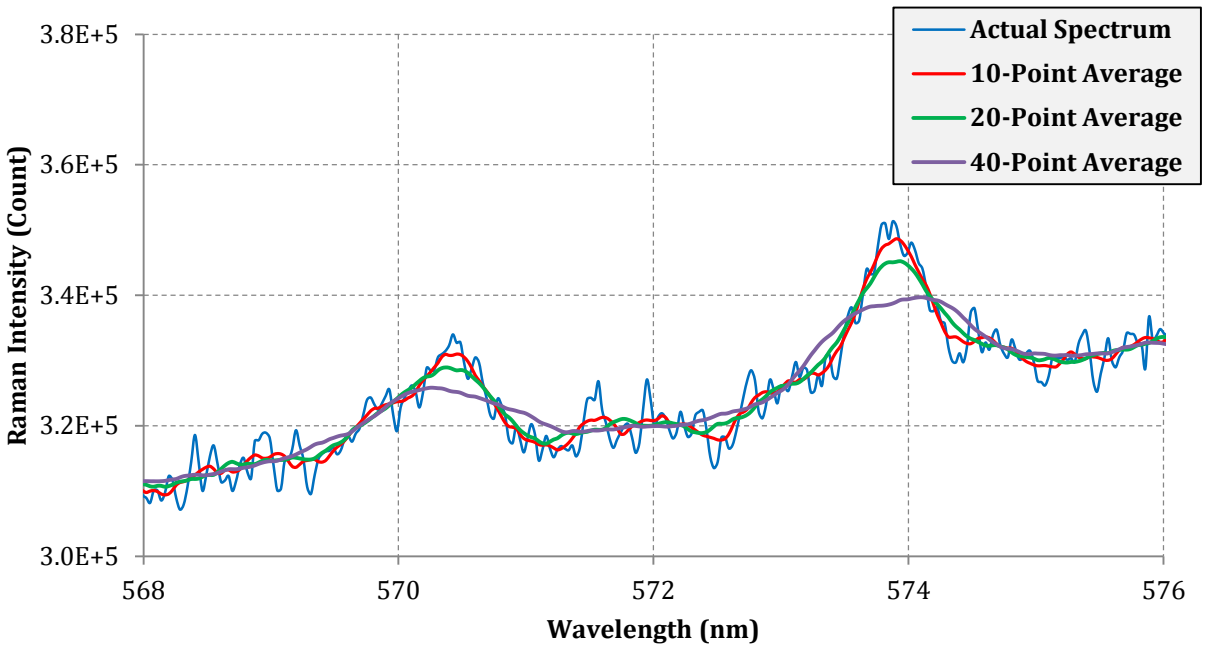

Figure 4.2 – Raman spectrum (20% CO_2 by volume at 104°C)

As shown in Figs. 4.1 and 4.2, there was an approximately 0.5 nm offset in the spectrum and as a result the peaks were located at 570.5 nm and 573.9 nm (instead of 571 nm and 574.4 nm). For a reason that has not been understood fully the background level of the spectra is relatively strong. In order to account for the effect of this background, a 2nd order polynomial was fitted to the curve excluding the points representing the peaks (569.5–571.5 nm and 572.5–575.5 nm). Because the lineshape of both measured CO_2 lines is closely similar, it is reasonable to expect that the full width at half maximum (FWHM) of the two lines is closely equal to the ratio of the corresponding intensities, which is 2:3 (571 nm line/ 574.4 nm line). Figure 4.3 shows the actual spectrum, smoothed spectrum and the 2nd order polynomial curvefit for 20% CO_2 by volume at 104°C. Fig. 4.4 shows the same result over a narrower range of wavelengths.

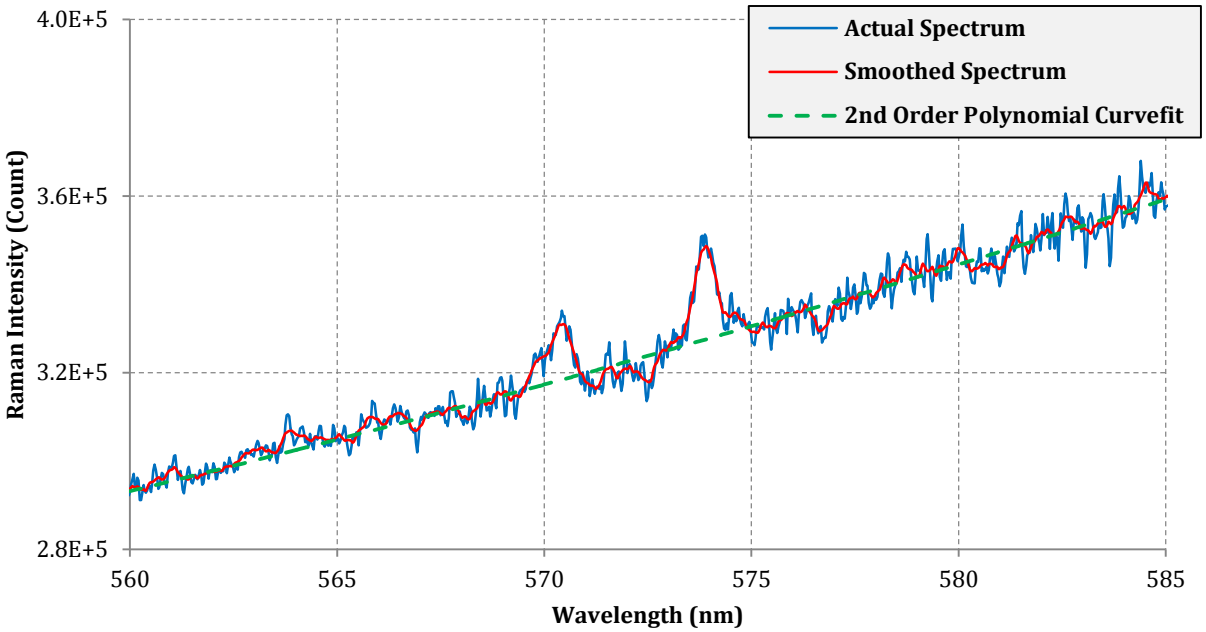

Figure 4.3 – Raman Spectrum (20% CO_2 by volume at 104°C)

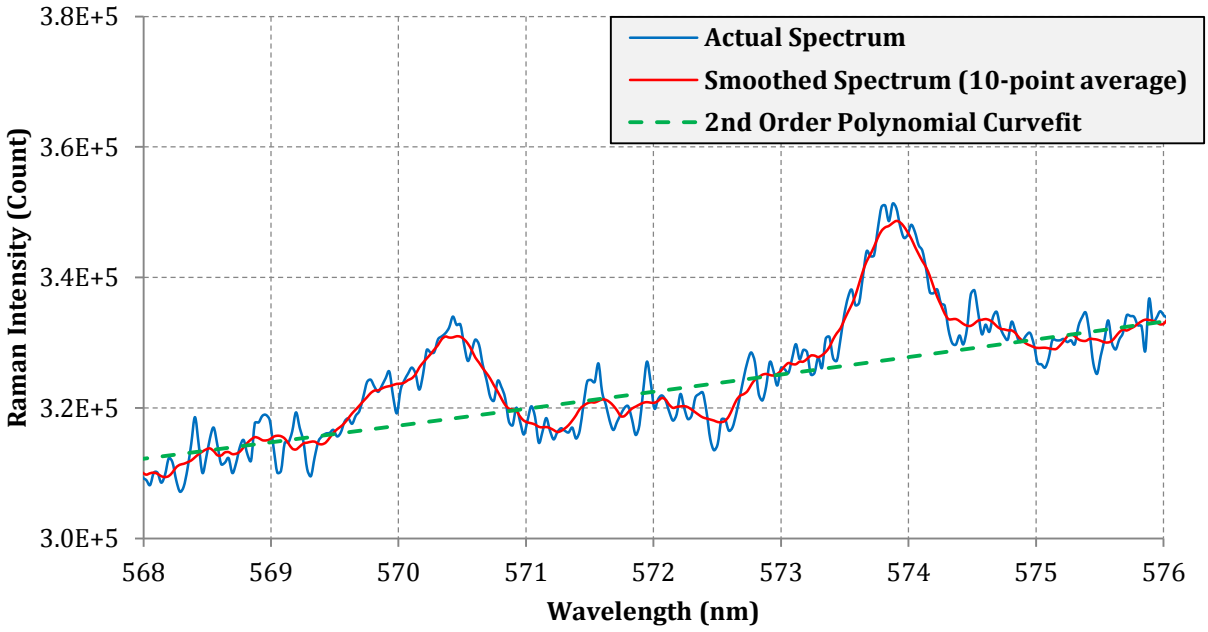

Figure 4.4 – Raman Spectrum (20% CO_2 by volume at 104°C)

The calculated polynomial was then subtracted from the smoothed spectrum, and all resulting negative values were replaced by zeros. Fig. 4.5 shows the processed spectrum for 20% CO_2 by volume at 104°C.

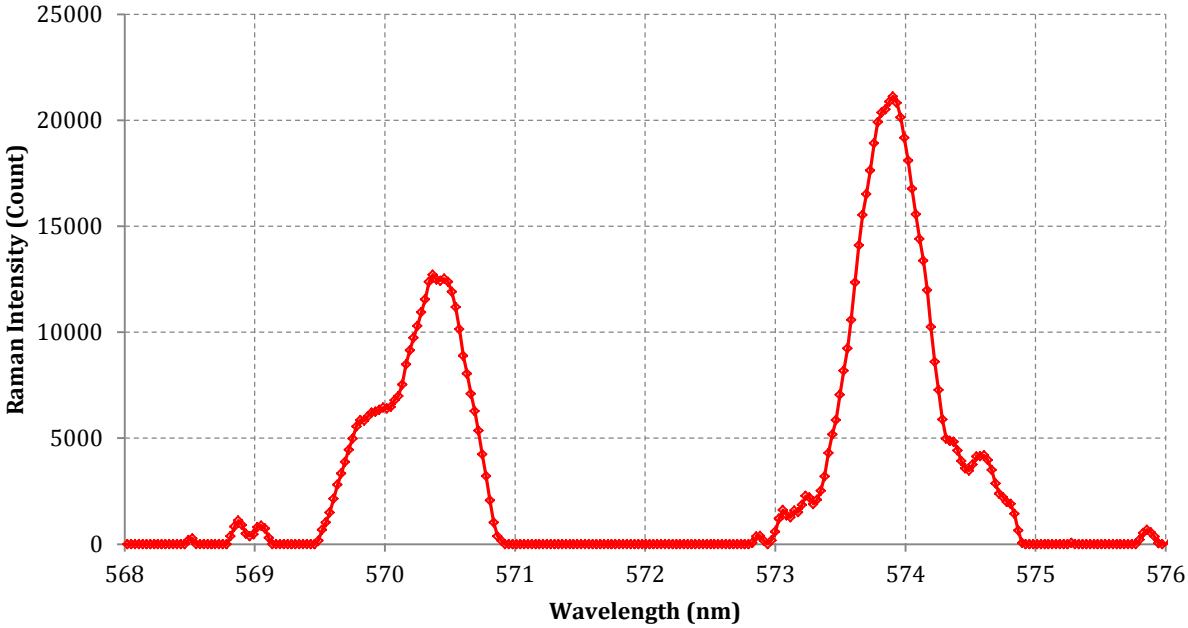

Figure 4.5 – Processed Raman Spectrum (20% CO_2 by volume at 104°C)

The integrated area under the two peaks was then used as the raw signal for comparing different spectra. The integration bandwidths used were 2 nm for the 571 nm peak (569.5–571.5 nm) and 3 nm for the 574.4 nm peak (572.5–575.5 nm). Figures 4.6 and 4.7 show Raman scattering intensity as a function of temperature and CO_2 concentration.

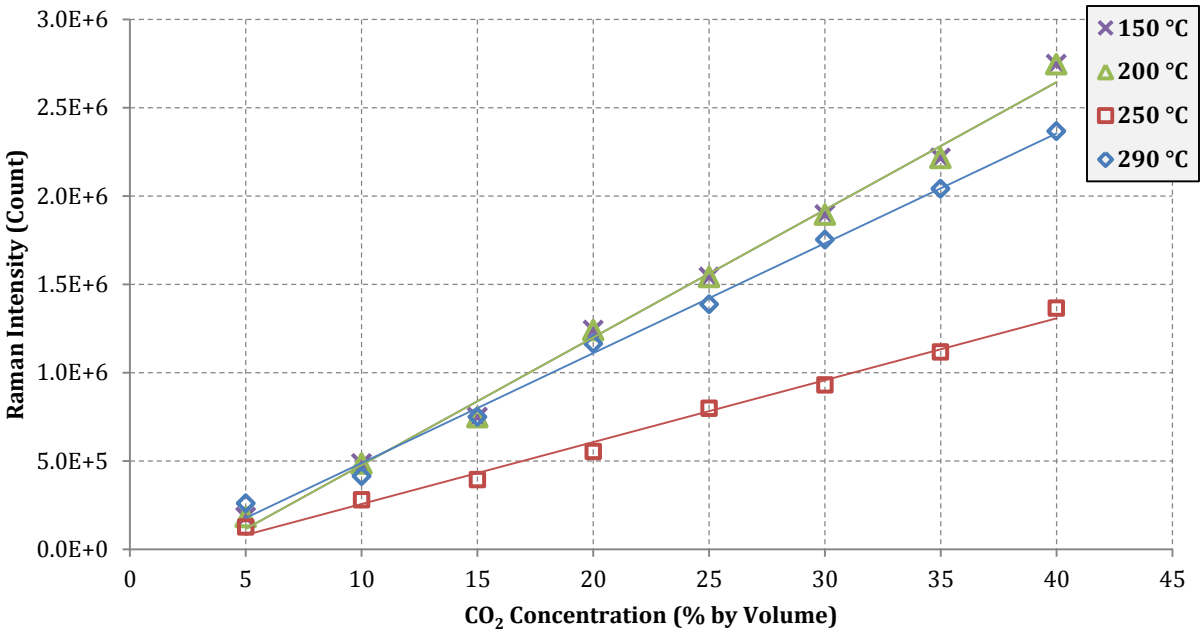

Figure 4.6 – Raman Intensity vs. Concentration for CO_2

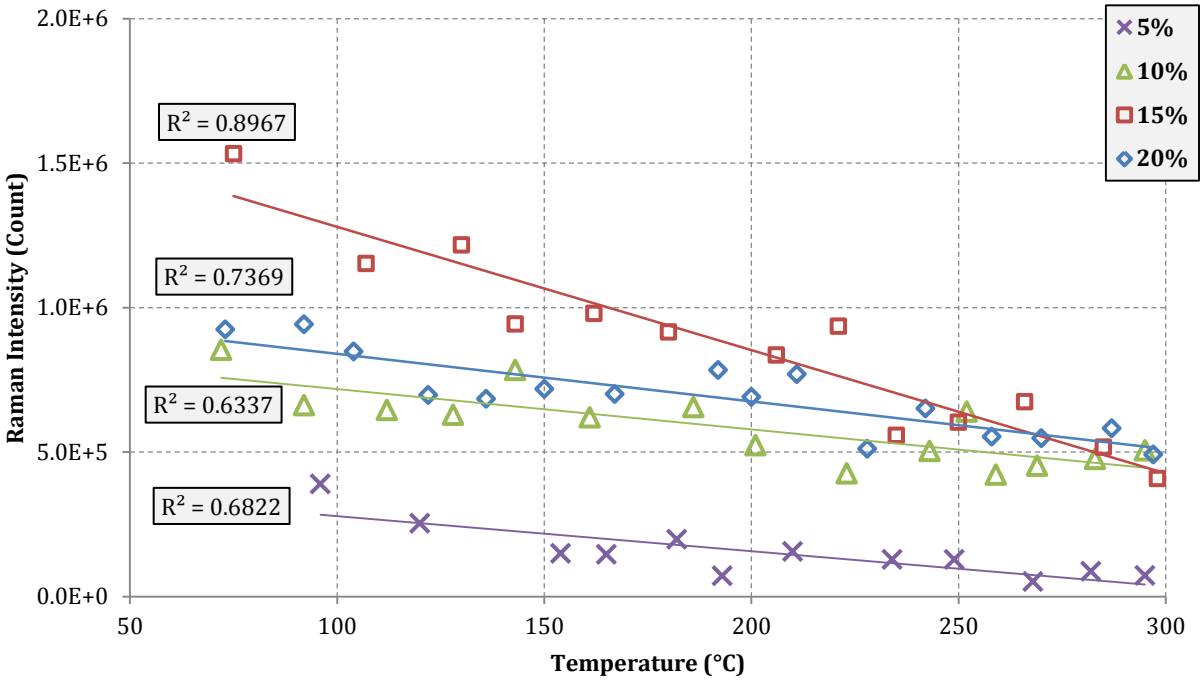

Figure 4.7 – Raman Intensity vs. Temperature for CO_2

Eckbreth [5] suggests that the power of the Raman signal can be calculated from a relation of the form,

$$P_r = kP_i nf(T) \tag{4.1}$$

where P_r is the measured Raman intensity, k is a factor that depends on geometry, species and optical setup, P_i is the incident laser intensity, n is the number density of the scattering species and $f(T)$ is the bandwidth factor which is a temperature-dependent term. So if the temperature and laser power are kept constant, and the optical setup is not changed, the Raman Stokes intensity will then be proportional to the number density (and concentration), which is evident in Fig. 4.6.

Figure 4.7 shows experimental measurements of Raman scattering intensity with temperature at various constant CO_2 concentrations. According to these results, Raman scattering intensity does not very monotonically with temperature. However, based on Fig. 4.7 the general trend is that at constant concentration, the Raman scattering intensity decreases as temperature increases. As shown in Fig. 4.9, the peak intensity dropped and the peaks became slightly broader with increasing temperature.

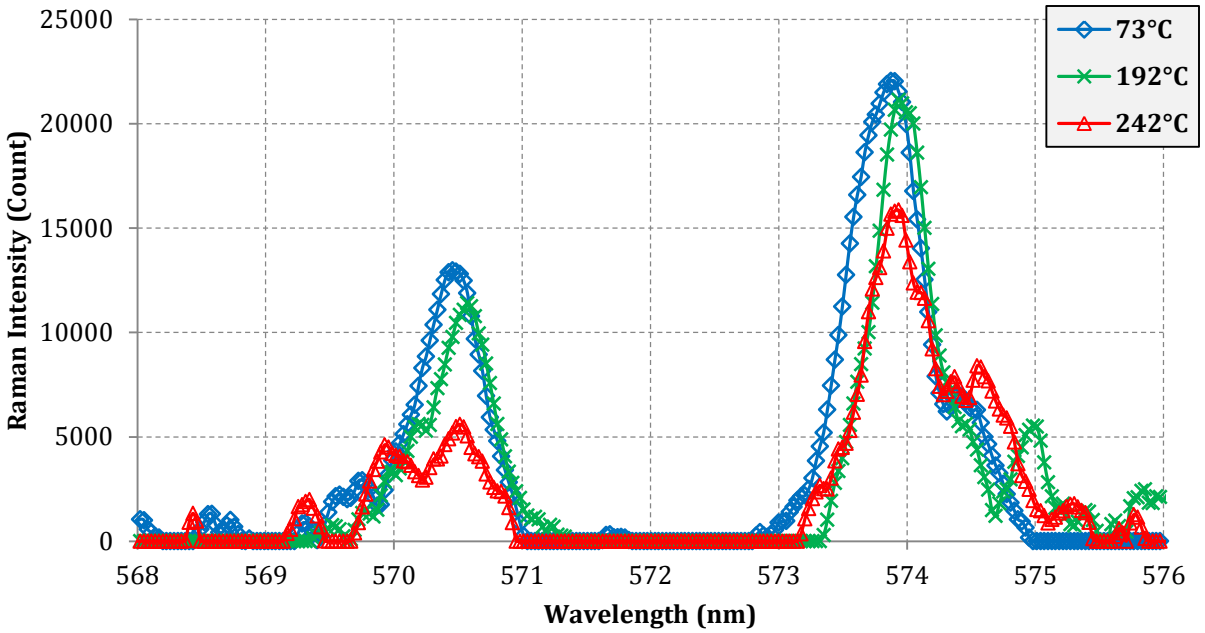

Figure 4.8 – Processed Raman spectra for 20% by volume CO_2 at different temperatures

Nevertheless, it should be mentioned here that the number density *does* change when temperature changes at constant pressure. So on the right hand side of Eq. 4.1, both n and $f(T)$ vary with temperature. However, the relation between n and T can be obtained from thermodynamics. From the ideal gas law,

$$p = n\bar{R}T \tag{4.2}$$

where p is the pressure, n is the number density, $\bar{R}$ is the ideal gas constant and T is the temperature. In our experiments, the pressure was constant and equal to the atmospheric pressure. Rearranging Eq. 4.2 shows that the number density is inversely proportional to the temperature:

$$n = \frac{p}{\bar{R}} \cdot \frac{1}{T} \tag{4.3}$$

Thus, with constant concentration, n drops as T increases. So, the decrease in Raman intensity with increasing temperature in Fig. 4.7 could be attributed in part to this effect. In

order to account for this effect, Raman intensity can be multiplied by absolute temperature. In this way, Raman scattering can be compared between samples with the same number density.

Replacing n in Eq. 4.1 from Eq. 4.3 yields:

$$P_r = kP_i \cdot \left(\frac{p}{\bar{R}} \cdot \frac{1}{T}\right) \cdot f(T) \tag{4.4}$$

An expression for the bandwidth factor, $f(T)$, will be:

$$f(T) = \frac{\bar{R}}{P_i kp} \cdot TP_r$$

As stated earlier, in our experiments, P_i was kept constant. Also, k is a factor that depends on geometry, species and optical setup. So, it can also be considered to be constant, because the optical setup and the geometry were kept unchanged. Furthermore, p was equal to the atmospheric pressure. Thus, $\bar{R}$, P_i, k and p can all be incorporated in a new constant, K. Then $f(T)$ will be:

$$f(T) = KTP_r \qquad K = \frac{\bar{R}}{kp_{atm}P_i} \tag{4.5}$$

Figure 4.9 presents corrected Raman intensity (which is equivalent to $T * P_r$ or $f(T)/K$) versus temperature. It basically shows how the bandwidth factor varies with temperature. The results indicate that the dependence of $f(T)$ on temperature in the conducted experiment is very week, or in other words, the variations in Raman scattering intensity with temperature at constant number density is small. As shown in Fig. 4.8, the R^2 value for the linear regression of signal dependence on temperature for CO_2 mole fractions of 10% and 15% is very close to zero. It should be noted that the use of R^2 value can be a little

misleading here, because a small R^2 value does not necessarily mean a low quality curvefit. In fact, $R^2=0$ corresponds to a constant horizontal curvefit whose value is equal to the average of the y-coordinates of the data points.

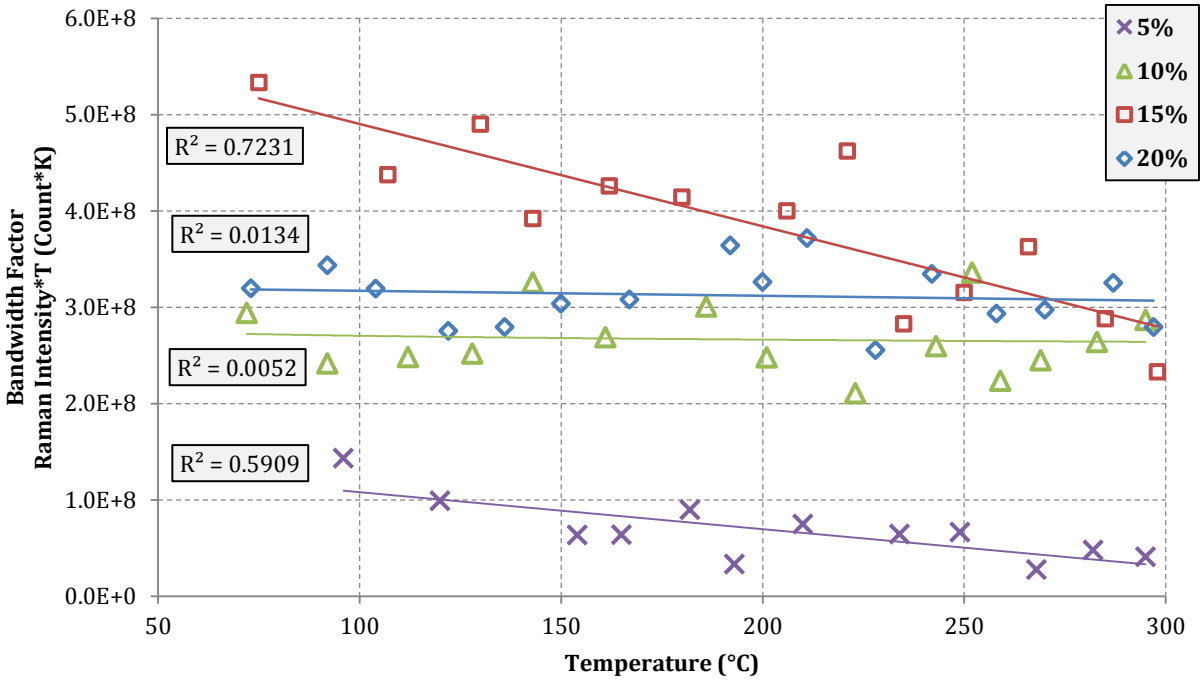

Figure 4.9 – Corrected Raman Intensity vs. Temperature for CO_2

In fact, the behavior of $f(T)$ also depends on the chosen filter bandwidth; i.e. the width of the peak used to measure the Raman signal. Figure 4.10 presents a Raman line of a hypothetical molecule at three different temperatures. It also shows two filters with different bandwidths.

For a narrow bandwidth filter (Filter 1 in Fig. 4.10), the fraction of total Raman scattering signal that is detected decreases as temperature increases, because part of the peak falls out of the filter bandwidth, and as a result $f(T)$ decreases. Thus, for a narrow bandwidth, $f(T)$ will decrease with increasing temperature.

On the other hand, for a certain bandwidth (Filter 2 in Fig. 4.10), the fraction of total Raman scattering signal detected stays almost constant. For such a configuration, the dependence of $f(T)$ on temperature is very weak.

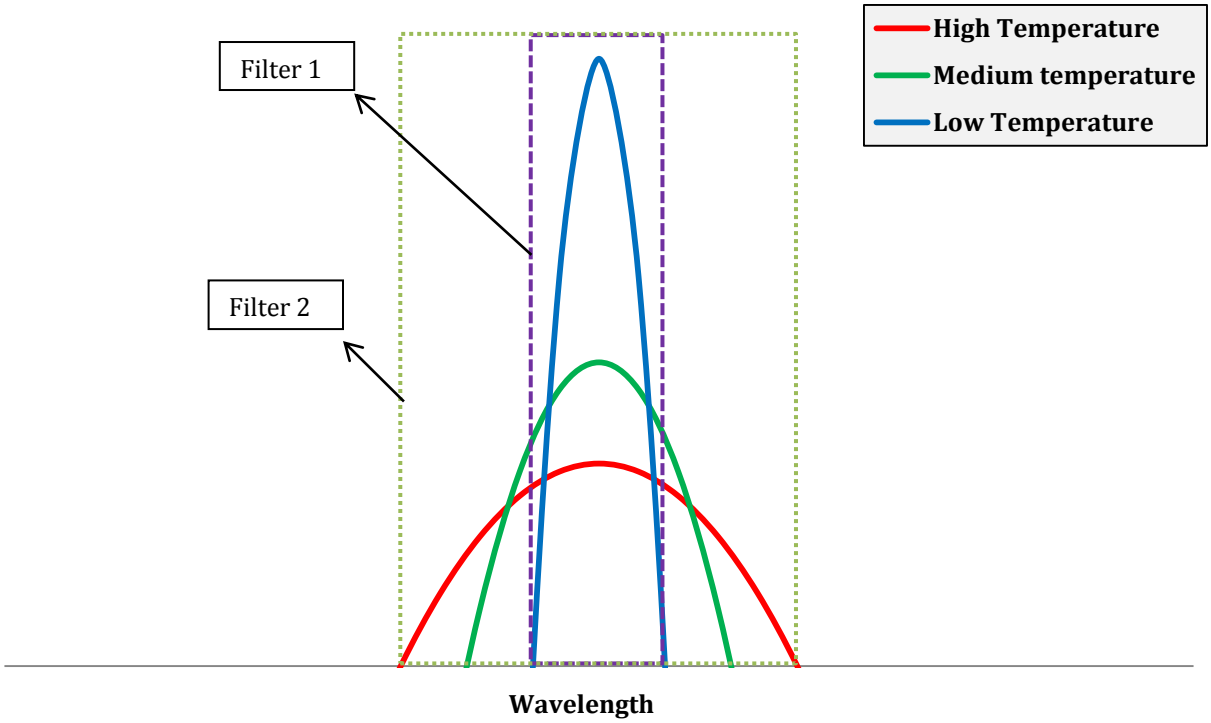

Figure 4.10 – Hypothetical Raman spectrum at different temperatures

Figure 4.11 shows the bandwidth factor versus temperature for 20% CO_2 by volume for four different bandwidths that were used for signal integration. The legend indicates the bandwidths chosen for the 571 nm and 574.4 nm peak respectively. For example, the "0.5 nm, 0.75 nm" data come from an integration from 570.25 nm to 570.75 nm for the 571 nm line and from 573.52 nm to 574.27 for the 574.4 nm line (remember that the spectrum was offset by 0.5 nm). The 2:3 bandwidth ratio was maintained for all four cases. In the fourth case, the bandwidths were the largest possible ones for which the areas of integration around the two peaks did not overlap. According to the results, the bandwidth factor

decreases as the bandwidth becomes narrower at constant temperature. Also, as temperature increases, the decrease in bandwidth factor is more noticeable for narrow bandwidths than for wide ones.

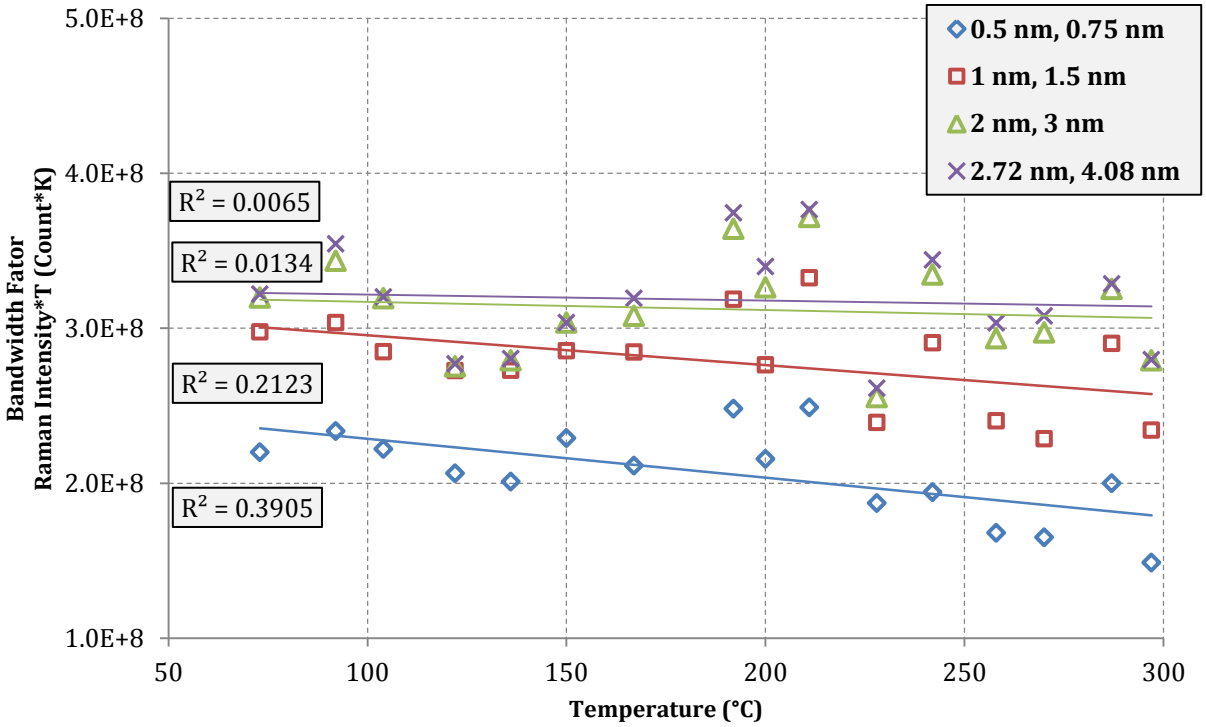

Figure 4.11 – Bandwidth Factor

Figure 4.12 shows the Raman scattering intensity versus infrared intensity for CO_2. These data were obtained by getting the Raman signal and infrared emission of CO_2 containing jets at constant temperature over the range of 5-40% concentration of CO_2 by volume with a 5% increment. Raman and infrared measurements were not simultaneous and were carried out independently. The integration bandwidth used for the Raman signal was 2 nm and 3 nm for the 571 nm peak and the 574.4 nm peak respectively.

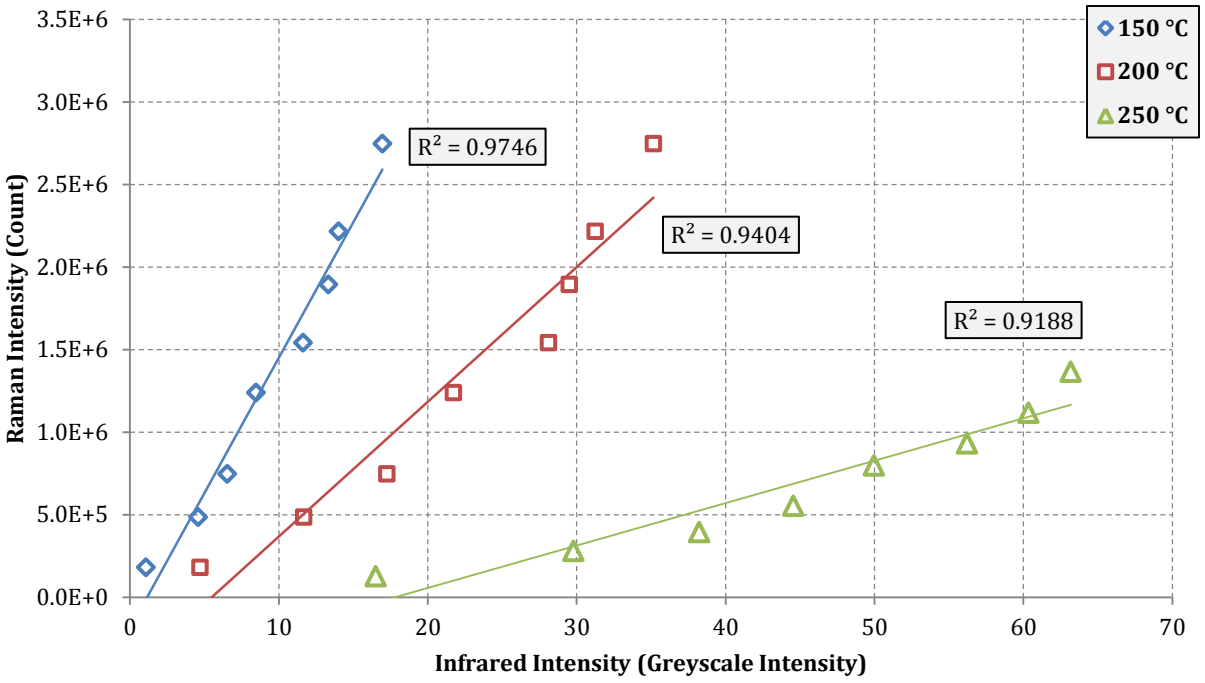

Figure 4.12 – Raman Intensity vs. Infrared Intensity

It is observed that at constant temperature, Raman intensity varies linearly with infrared intensity to a very good approximation. This further signifies the relationship between Raman scattering and infrared activity. In fact, Raman scattering and infrared activity both stem from the same the source, which is the vibrational structure of the molecule.

Chapter 5: Summary, Conclusions and Recommendations

5.1 Summary and Conclusions

Raman scattering spectrum and infrared emission intensity in CO_2-containing atmospheric jets at various temperatures and concentrations were measured. The results indicated that the infrared emission intensity from CO_2-containing jets increased linearly with CO_2 concentration at constant temperature. Also, the infrared emission intensity increased with temperature at constant concentration in manner that was very closely described by 4^{th} order polynomials. Measured infrared emission intensities were compared to numerical simulations from the RADCAL code of NIST and good agreement was established.

The results of Raman scattering measurements indicated that Raman scattering intensity increased linearly with concentration at constant temperature, which was expected from theory [5]. On the other hand, Raman scattering intensity decreased with temperature at constant concentration. It was established that, this decrease was partly due to the increase in temperature that decreased the number density. In order to resolve this issue, Raman signal intensity multiplied by absolute temperature was also recorded. This quantity is equivalent to the bandwidth factor, $f(T)$, defined by Eckbreth [5]. The results showed that the bandwidth factor was only weakly dependent on temperature. The effect bandwidth on the integration of spectra was systematically evaluated and an optimal bandwidth was determined for data processing.

Finally, Raman scattering results taken at constant temperature for CO_2 mole fractions of 5-40% with a 5% increment were correlated with the corresponding infrared emission data. The results indicated that the Raman scattering intensity increased linearly with infrared emission intensity to a very good approximation, which points to the potential importance of Raman as a technique for the measurement of greenhouse activity.

The results of this work show that it is possible to use the Raman scattering technique to measure greenhouse gases. This is because Raman scattering and infrared activity stem from the same source, which is the rotational and vibrational molecular motion. Moreover, the linear dependence of Raman signal on concentration as well as infrared emission intensity points to the fact that Raman scattering can be a strong technique for measurement of greenhouse gases.

5.2 Recommendations for Future Work

The results presented in this work provide a preliminary framework for study of a Raman based measurement of greenhouse gases. Due to the high noise level of the ICCD camera used, it was not possible to obtain reliable data for CO_2 mole fractions less than 5%. Also it was not possible to take data for more closely spaced mole fractions. For the purpose of this experiment, a non-intensified CCD camera will be much more appropriate than the intensified CCD camera used. Intensifiers are a “must” for applications with high background luminosity; e.g. flames. However, they are inherently noisy devices and not very suitable for the application considered here.

In order to improve the signal-to-noise ratio, a multipass optical setup could be employed. The configuration described by Hill and Hartley [27] can result in two orders of magnitude increase in scattered signal intensity. The setup used by Hill and coworkers is simpler compared to the former setup and can provide gains of 20-30 [28]. Placing a spherical mirror in line with the collection lens, on the opposite side of the probe volume can double the solid angle and hence the signal intensity [5].

In a more efficient optical setup with a non-intensified CCD camera, possibility of single-shot Raman measurements can be investigated as well. Such a technique can be used for instantaneous in situ measurement of greenhouse gas emissions.

In this work CO_2 was studied which is the greenhouse gas that is under the most serious consideration in the context of greenhouse gas emissions and global warming. Future work could include other greenhouse gases such as CH_4, H_2O, NO, CO, etc.

References

1. ASTM-G173-03 Reference Spectra, American Society for Testing and Materials (ASTM) Terrestrial Reference Spectra for Photovoltaic Performance Evaluation.
2. Cengel, Y. A., and A. J. Ghajar, *Heat and Mass Transfer: Fundamentals & Applications*, 4th edition. New York: McGraw-Hill, 2011.
3. Atkins, P., and J. de Paula, *Physical Chemistry*, 8th edition. Great Britain: Oxford University Press, 2006.
4. Long, D. A., *Raman Spectroscopy*. Great Britain: McGraw-Hill, 1977.
5. Eckbreth, A. C., *Laser Diagnostics for Combustion Temperature and Species*, 2nd edition. New York: Taylor & Francis, 1996.
6. Lapp, M., and D. L. Hartley, Raman Scattering Studies of Combustion. *Combustion Science and Technology* 13 (1976): 199-210.
7. Stephenson, D. A., High-temperature Raman Spectra of CO_2 and H_2O for Combustion Diagnostics. *Applied Spectroscopy* 36.6 (1981): 582-584.
8. Aeschlim, D. P., j. C. Cummings, and R. A. Hill, Raman Spectroscopic Study of Laminar Hydrogen Diffusion Flame in Air. *Journal of Quantitative Spectroscopy and Radiative Transfer* 21 (1979): 293-307.
9. Blint, R. J., and D.A. Stephenson, Carbon Dioxide Concentration and Temperature in Flames by Raman Spectroscopy. *Journal of Quantitative Spectroscopy and Radiative Transfer* 23 (1980): 89-94.

10. Schoenung, S. M., and R. E. Mitchell, Comparison of Raman and Thermocouple Temperature Measurements in Flames. *Combustion and Flame* 35 (1979): 207-211.
11. Long, M. B., B. F. Webber, and R. K. Chang, Instantaneous Two-Dimensional Concentration Measurements in a Jet Flow by Mie Scattering. *Applied Physics Letters* 34 (1979): 22-24.
12. Long, M. B., D. C. Fourguette, M. C. Escoda, and C. B. Layne, Instantaneous Ramanography of a Turbulent Diffusion Flame. *Optics Letters* 8 (1983): 244-246.
13. Long, M. B., P. S. Levin, and D. C. Fourguette, Simultaneous Two-Dimensional Mapping of Species Concentration and Temperature in Turbulent Flames. *Optics Letters* 10 (1985): 267-269.
14. Kyritsis, D. C., P. G. Felton, Y. Huang, and F. V. Bracco, Quantitative two-dimensional instantaneous Raman concentration measurements in laminar methane jet. *Applied Optics* 39.36 (2000): 6771:6780.
15. Kyritsis, D. C., P. G. Felton, and F. V. Bracco, Instantaneous, Two-dimensional, spontaneous Raman measurements of hydrogen number density in a laminar jet using an intra-cavity configuration. *International Journal of Alternative Propulsion* 1.2 (2007): 174-189.
16. Karpetis, A. N., T. B. Settersten, R. W. Schefer, and R. S. Barlow, Laser imaging system for determination of three-dimensional scalar gradients in turbulent flames. *Optics Letters* 29 (2004): 355-357.
17. Karpetis, A. N., and R. S. Barlow, Measurements of scalar dissipation in a turbulent piloted methane/air jet flame. *Proceedings of the Combustion Institute* 29 (2002): 1929-1936.

18. Barlow, R. S., and A. N. Karpetis, Measurements of scalar variance, scalar dissipation, and length scales in turbulent, piloted methane/air jet flames. *Flow Turbulence and Combustion* 72 (2004): 427-448.

19. Barlow, R. S., et al, Piloted jet flames of CH_4/H_2/Air: Experiments on localized extinction in the near field at high Reynolds numbers. *Combustion and Flame* 156 (2009): 2117-2128.

20. Wang, G., A. N. Karpetis, and R. S. Barlow, Dissipation length scales in turbulent non-premixed jet flames. *Combustion and Flame* 148 (2007): 62-75.

21. Bijjula, K., and D. C. Kyritsis, Experimental evaluation of flame observables for simplified scalar dissipation rate measurements in laminar diffusion flamelets. *Proceedings of the Combustion Institute* 30 (2005): 493-500.

22. Smyth, S. A., K. Bijjula, and D. C. Kyritsis, Intermediate Reynolds/Peclet number, flat plate boundary layer flows over catalytic surfaces for micro-combustion applications. *International Journal of Alternative Propulsion* 1.2 (2007): 294-308.

23. Agathou, M. S., and D. C. Kyritsis, An experimental comparison of non-premixed bio-butanol flames with the corresponding flames of ethanol and methane. *Fuel* 90 (2011): 255-262.

24. Incropera, F. P., et al, *Fundamentals of Heat and Mass Transfer*, 6th edition. New York: John Wiley & Sons, Inc., 2007.

25. Herzberg, G., *Molecular Spectra and Molecular Structure.* Lancaster, PA: Lancaster Press, Inc., 1966.

26. Grosshandler, W. L., RADCAL: A Narrow-Band Model for Radiation Calculations in a Combustion Environment. *NIST Technical Note 1402*, 1993.

27. Hill, R. A., and D. L. Hartley, Focused, Multiple-Pass Cell for Raman Scattering. *Applied* Optics 13.1 (1974):186-192.

28. Hill R. A., A. J. Mulac, and C. E. Heckett, Retroreflecting Multi-pass Cell for Raman Scattering. *Applied Optics* 16 (1977): 2004-2006.